MATERIALS SCIENCE

Dome-celled aerogels with ultrahigh-temperature superelasticity over 2273 K

Kai Pang[1]†, Yuxing Xia[1]†, Xiaoting Liu[1]†, Wenhao Tong[2]†, Xiaotong Li[1], Chenyang Li[1], Wenbo Zhao[1], Yan Chen[2], Huasong Qin[2], Wenzhang Fang[1], Li Peng[1], Yilun Liu[2], Weiwei Gao[1], Zhen Xu[1]*, Yingjun Liu[1]*, Chao Gao[1]*

Aerogels are known for their high porosity and very low density and can be made from a range of materials, but are limited by structural instability under extreme thermomechanical conditions. We report on 194 types of dome-celled ultralight aerogels that maintain superior elasticity spanning from 4.2 kelvin (K) to 2273 K, realized by a two-dimensional channel–confined chemistry method. Such aerogels exhibit superelasticity under 99% strain for 20,000 cycles and thermal shock resistance at 2273 K over 100 cycles. The high-entropy carbide aerogel achieves a thermal conductivity of 53.4 $mW{\cdot}m^{-1}{\cdot}K^{-1}$ at 1273 K and 171.1 $mW{\cdot}m^{-1}{\cdot}K^{-1}$ at 2273 K. The combination of temperature-invariant elasticity and chemical diversity makes such aerogels highly promising for extreme thermomechanics, from heat-insulated industries to deep space exploration.

Aerogels have emerged as an important family of materials that feature high porosity and low density, which enables a wide range of applications in space exploration, sensing, thermal management, and chemical catalysis (*1*–*4*). Various aerogels have been progressively synthesized using the conventional sol-gel method, spanning metals, oxides, chalcogenides, carbides, carbons, organics, and multinary compounds (*4*–*13*) (table S1). However, most sol-gel aerogels tend to exhibit mechanical brittleness and poor elasticity due to their intrinsic weak zero-dimensional granular connections (*4*, *5*).

To overcome the intrinsic weakness of aerogels, a geometrical design of structures has been developed to achieve outstanding mechanical elasticity at high porosity, typically through intertwining one-dimensional fibers or nanotubes (*14*–*20*), and assembling two-dimensional (2D) nanosheets to honeycomb and arched cell structures, as well as the formation of macroscopic hyperbolic meta-patterns (*21*–*26*) (table S2). Despite these advances, aerogels still face challenges in maintaining thermomechanical stability under extreme thermal and mechanical conditions due to unstable crystalline structure at high temperatures and the structural fragility under large mechanical deformation (*4*, *27*).

The flexible amorphous domain is a crucial component for maintaining the elasticity of ceramic aerogels at normal conditions, but its presence considerably lowers their thermal stability compared with bulk crystalline ceramics. Previous efforts to improve thermal stability of elastic ceramic aerogels have primarily focused on restricting the migration of amorphous domains, which achieved a maximum working temperature of 1973 K (*27*). Although graphene materials exhibit melting points exceeding 3000 K, their mechanical softening temperature is limited to below 2273 K (*28*), precluding stable thermomechanical performance under such extreme conditions.

Aerogel fabrication

We report a general 2D channel–confined chemistry method to synthesize a series of ultralight dome-celled aerogels across hundreds material species, covering 121 oxide, 38 carbide, and 35 metal species, with compositions tunable to high-entropy states containing up to 30 elements. We propose a dome microstructure with two nonzero principal curvatures (κ_1 and κ_2, fig. S1) as basic cells, introducing curvature as an alternative structural parameter for aerogel design. The dome structure, commonly found in biology and architectural engineering, is well known for its excellent load-bearing capacity and mechanical stability (fig. S2). Finite element analysis reveals that a dome exhibits a capability for storing elastic strain energy that is at least 10 times greater than that of conventional honeycomb and arch structures (fig. S3). This becomes more pronounced for aerogels with thinner cell walls, as it generates richly recoverable wrinkles to store elastic energy (fig. S4), due to its undevelopable surface characteristics. This comparative analysis demonstrates that the dome structure is a preferable geometric design for ultralight aerogels, potentially enabling superior elasticity under large deformation.

Experimentally, we used a general 2D channel–confined chemistry method to prepare dome-celled aerogels, starting from macroscopic assembled graphene oxide (GO) films. The method is continuously processed by three steps: ion capturing, bubbling, and heat conversion (Fig. 1A). GO was chosen as a 2D channel precursor because of its abundant chemical moieties, atomic thickness, and large-scale commercial availability (*29*), exhibiting high compatibility for fabricating dome-celled aerogels. Water easily penetrates into GO interlayer channels, forming a 2D confined nanospace with distance (d) from 0.97 to 2.14 nm (fig. S6A). When immersed in salt solutions (single or multiple ion species up to 30 kinds), the diffused ions are captured into GO interlayer channels by chelation interaction with oxygen functional groups (*29*) and the 2D barrier effect allows avoidance leakage of ions (*30*), forming confined precursor hybrids. The GO-ion hybrid exhibited an atomic uniformity in hybridization, as shown by x-ray diffraction (XRD) (single peak at 6.2°; fig. S6B) and homogeneous elemental distribution in interlamination, whether single or multiple ions (figs. S7 and S8).

Decomposing gas from the foaming reagent generates bubbles in the GO interlayer gallery (*31*), forming cells with a dome shape that contribute to the flexibility of GO-ion laminates. The dome cells inherit the non-Euclidean curvature of spherical bubbles, distinct from the regular polyhedral cell formed by the conventional ice templating method (*16*, *23*–*26*). By controlling the pressure by bubbling time, the average curvature (K_a) of dome cells is tuned from 0.045 to 0.122 μm^{-1} (fig. S9). Our hybrid aerogels were prepared by direct drying in air, avoiding the complex and costly freeze or supercritical drying methods (*4*).

We thermally treated the hybrid aerogels at 600°C for 4 hours with air to remove GO and yield neat oxide aerogels with dome-celled microstructures, extending from unary to high-entropy constituents. We used XRD, x-ray photoelectron spectroscopy, energy dispersive spectroscopy, special aberration correlated transmission electron microscopy (AC-TEM), and atomic mapping to demonstrate the confined formation mechanism that preserves the dome shape (figs. S6 to S8). Taking the Al_2O_3 aerogel as an example, atomically dispersed Al^{3+} ions in 2D confined channels gradually transform into polycrystalline oxide lamella by forming interconnected nanocrystals (fig. S10), instead of large-sized crystallite aggregates without confinement (*32*). For complex combinations of elements, local confined ions (such as Al, Ti, Cr, Co, and Ni) form polycrystalline oxide lamellae with high mixing homogeneity across a micrometer scale at minimum (fig. S11). By contrast, annealing ions only absorbed on GO surface forms coarse oxide

[1]MOE Key Laboratory of Macromolecular Synthesis and Functionalization, International Research Center for X Polymers, Zhejiang Key Laboratory of Advanced Organic Materials and Technologies, Research Center for Advanced Fibers, Department of Polymer Science and Engineering, Zhejiang University, Hangzhou, China. [2]Laboratory for Multiscale Mechanics and Medical Science, SV LAB, School of Aerospace, Xi'an Jiaotong University, Xi'an, China. ***Corresponding author. Email: zhenxu@zju.edu.cn (Z.X.); yingjunliu@zju.edu.cn (Yin.L.) chaogao@zju.edu.cn (C.G.)** †These authors contributed equally to this work.

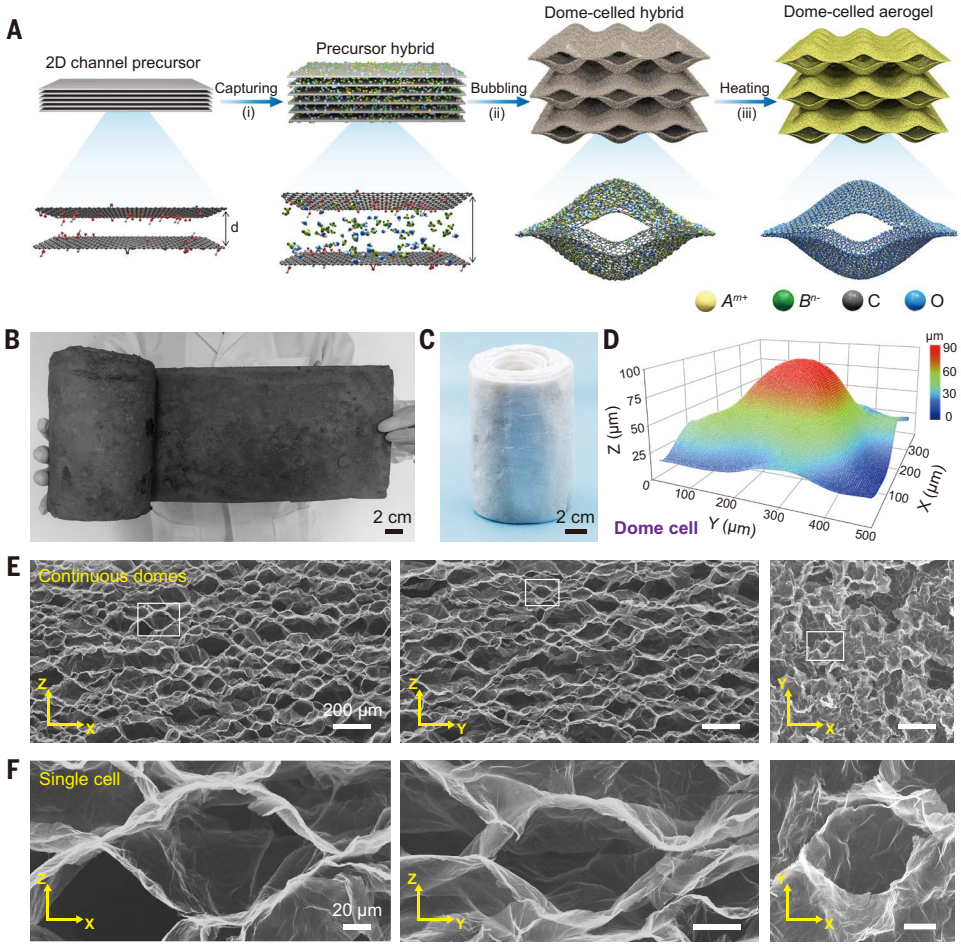

Fig. 1. Graphene-based 2D channel–confined chemistry for dome-celled aerogels. (**A**) Preparation of aerogels from the 2D channel precursor in three steps: (i) Salt ions are captured by the tunable GO channels; (ii) the solvent bubbling with foaming agent is adopted to fabricate a dome-celled hybrid; and (iii) the heat conversion process is conducted at 600°C in air for 4 hours, 2000°C in an argon atmosphere for 2 hours, or 450°C in a hydrogen atmosphere for 1 hour, to fabricate oxide, carbide, or metal aerogels, respectively. (**B** and **C**) Digital photos of as-prepared carbide plate and oxide roll aerogels. (**D**) 3D optical image of a dome cell model made by bubbling an ultrathin GO film (~500-nm thickness). (**E** and **F**) SEM analysis of dome-celled aerogel from slicing images in three directions (the X-Z, Y-Z, and X-Y planes).

crystallites, leading to the collapse of dome cells (fig. S12). By pairing species and controlling proportion of captured ions, we obtained high-entropy oxide aerogels (fig. S13 and table S3). Subsequently, the oxide aerogels were thermally reduced into metal ones by hydrogen at 450°C for 2 hours. Additionally, thermal annealing of second-step hybrid aerogels at 2000°C for 2 hours in argon activated the reaction between oxide and graphene, resulting in carbide aerogels. Alternatively, the graphene framework can be retained in these aforementioned aerogels by controlling the GO/ion ratio and heating atmosphere.

Based on the GO films, we prepared aerogel bricks of oxide, carbide, and metal members. To meet more practical application demands, other macroscopic aerogel forms of large-scale plates (~50×20×0.5 cm^3) and continuous rolls (>2 m) (Fig. 1, B and C, and fig. S14), were obtained.

We performed 3D optical profilometer and x-ray nano-computed tomography (nano-CT) to validate the dome shape of the cells. A representative cell unit was extracted to illustrate the geometrical nature of the dome shape. The dome vertex has two orthometric positive Gaussian curvatures, interconnected by saddle-shaped edges (Fig. 1D, fig. S15, and movie S1). After heat treatment, the dome-celled aerogels maintained seamless contact between structural cells (fig. S16), ensuring their structural stability and integrity. When extended to the macroscale (Fig. 1, E and F), vertical (X-Z and Y-Z planes) and horizontal (X-Y plane) slicing of aerogel using both scanning electron microscope (SEM) and nano-CT confirmed the dome shape of cells. Dome cell sizes range from tens to hundreds of microns. Layer-by-layer nano-CT slicing further reveals that the interconnected dome cells are homogeneous across the millimeter scale (movie S2).

Broad chemical diversity

We synthesized hundreds of dome-celled aerogels (194 types) with broad chemical diversity, encompassing oxide, metal and carbide components, and involving more than 30 elements (Fig. 2A). The aerogels are sufficiently diverse to form a comprehensive library, including 20 unary, 30 binary, 30 ternary, and 41 high-entropy oxides; 8 unary, 10 binary, 10 ternary, and 10 high-entropy carbides; and 5 unary, 10 binary, 10 ternary, and 10 high-entropy metals (figs. S17 to S22). These aerogels feature ultralow density (ρ), ranging from 0.35 to 13.78 mg·cm^{-3}, irrespective of elemental composition. In the density spectrum, most of our aerogels fall within the extralight (ρ < 1.29 mg·cm^{-3} of air) and ultralight (ρ < 10 mg·cm^{-3}) ranges (fig. S23).

Figure 2, B to F shows representative oxide, carbide, metal, and high-entropy aerogels with hydrolytic stability (fig. S24), which can float on flower buds as a result of their lightness. All aerogels possess dome-celled structures, comprising 2D curved walls and micro-sized pores (70 to 140 μm; fig. S25), as observed in SEM vertical sections. The thin walls are composed of planar interconnected nanosized crystal grains (AC-TEM) and have a thickness <10 nm (fig. S26) resulting from the confined growth of the crystals (*33*). The ultrathin wall thickness contributes to the ultralow density of our aerogels. Detailed examinations reveal that oxide, carbide, and metal aerogels generally exhibit structural and compositional uniformity (figs. S27 to S34). To confirm the atomic-scale homogeneity in high-entropy cases, we used high-angle annular dark-field (HAADF) imaging and atomic mapping, finding that up to 30 arbitrary elements were thoroughly mixed at the atomic scale (figs. S21, S22, and S35 to S37). In these high-entropy aerogels (figs. S38 to S40), three similar elements at minimum were preferentially chosen to minimize the mixing enthalpy, and other additional elements were incorporated to further increase the mixing entropy (*34*, *35*).

Extreme thermomechanics

All aerogels in the library exhibited exceptional elasticity, regardless of chemical species, elemental compositions, and density. We first investigated the mechanical elasticity of our aerogels under quasistatic compression. Intuitively, a stack of oxide, carbide, and metal aerogels with ~30% retained graphene—ranging from unary to high-entropy components—was compressed at an extreme strain of 99% and fully

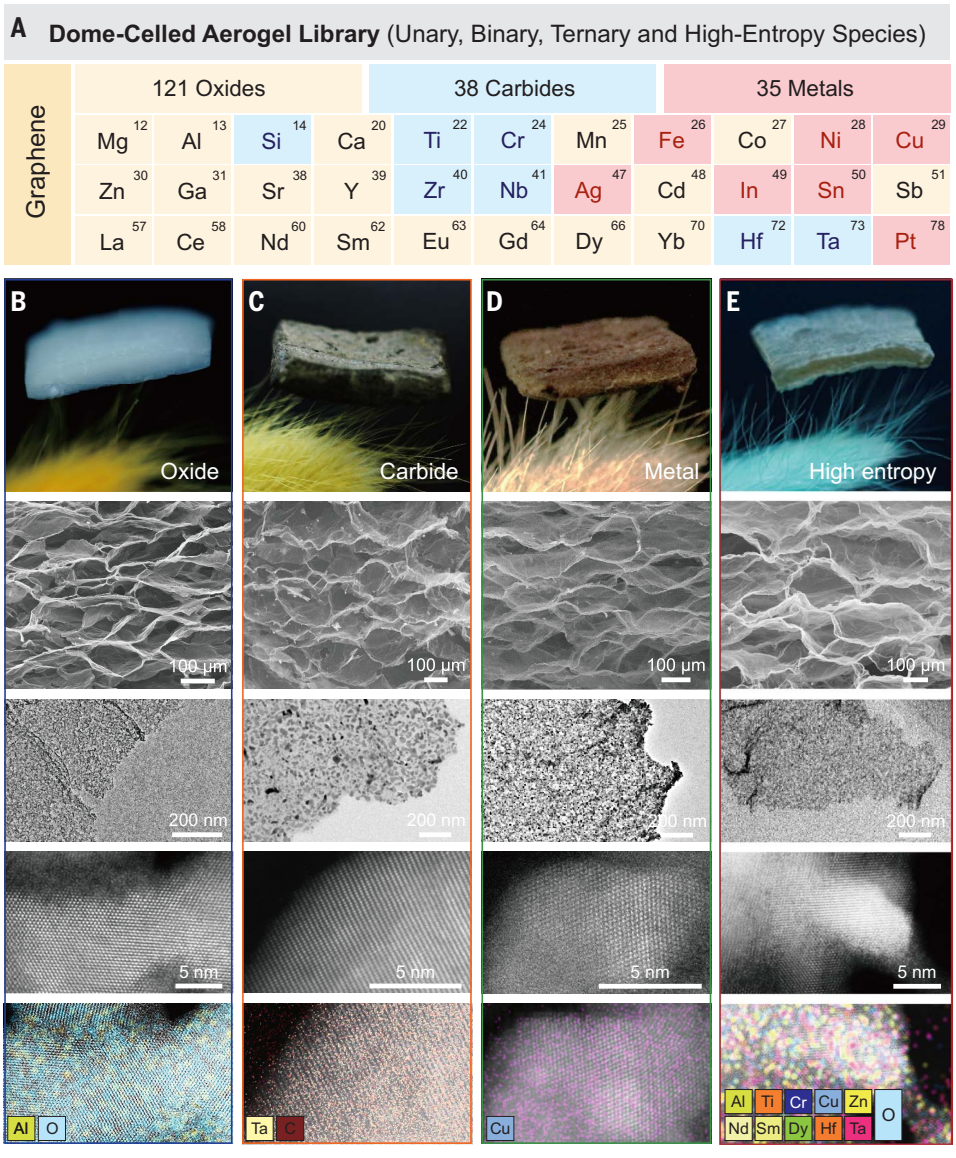

Fig. 2. Chemical diversity of dome-celled aerogels and their multiscale structures. (**A**) Elemental overview of the aerogel library for oxides (highlighted in yellow, except for Ag and Pt), carbides (highlighted in blue), and metals (highlighted in red). (**B** to **E**) Optical images of unary aluminum oxide (Al_2O_3), tantalum carbide (TaC), copper (Cu), and high-entropy denary AlTiCrCuZnNdSmDyHfTa oxide aerogels (from left), and their corresponding structure characterizations by SEM, AC-TEM, and HAADF atomic elemental mapping.

recovered to the original height after the pressure was released (Fig. 3A and movie S3). These aerogels could be repeatedly compressed at 99% strain for 20,000 cycles with nearly unchanged sample height (residual strain <3%) and minimal stress degradation (<20%). Extralight oxide aerogels (ρ of 0.35 to 1.24 mg·cm^{-3}) with compositions (Y_2O_3 and InSn, AlCrYLaCe, and MgAlCrMnFeCoNiCuSrYIn oxides) exhibiting stable elasticity and little strain degradation (<8%) at 80% strain up to 10,000 cycles (figs. S41 and S42 and movie S4), indicating excellent fatigue resistance.

We investigated the deformation behavior of the dome cell by in situ compression experiments. Under a 3D optical profilometer, the dome cell underwent doubly curved deformation in two principal directions (fig. S43), demonstrating the typical undevelopable surface nature of dome structures (fig. S1). In situ SEM observation shows that massive fine wrinkles emerged at higher strain (80%), which avoids the smooth and compact contact between nanowalls and favors the elastic recovery (Fig. 3B and movie S5). These experimental results validate the design rationale behind the dome cell as the expected aerogel structure for achieving high elasticity at ultralow density. By contrast, the flat walls of the honeycomb aerogel control sample were deformed along the longitudinal direction to form a smooth compact contact, resulting in its limited resilience (fig. S44, A to D). When scaled up, these dome cells became interconnected through a surface contact (Fig. 1 and fig. S15), efficiently transferring the load across the network (*31*) and enhancing the macroscopic elasticity of our aerogels, regardless of material components or heat treatment processes (fig. S44, E and F). By controlling cell curvature, we detected that larger curvature generates better mechanical resilience (fig. S45). When plotted on the elasticity-density map of aerogels (Fig. 3C and table S2), our aerogels not only exhibit exceptional mechanical recoverability under large strains (99%) but also break through the limits of elasticity at extreme lightness (*4*, *16*–*19*, *22*–*26*, *36*–*43*).

We investigated the crystalline structure of dome-celled carbide aerogels. On the dome wall, the carbide sheet nanograins are tightly inserted into graphene planar sheets in a mosaic pattern, (figs. S46 and S47). Below a carbide content of 88 weight percent (wt%), the carbide mosaic grains maintain a planar shape with lateral size increasing from the nanoscale (~5 nm) to the microscale (~50 nm), exhibiting confinement by graphene. Further mechanical tests (fig. S48, A to D) demonstrated dome-celled carbide aerogel with a carbide content <88 wt% displayed excellent mechanical recoverability under compressive strain of 90% in the vertical direction, surpassing its performance in the horizontal direction (fig. S49). By contrast, the freeze-dried honeycomb carbide aerogel (63 wt% carbide content) failed to recover to its original height at 90% strain after 10 cycles (fig. S48E), further highlighting the mechanical superiority of the dome-celled structure.

Under extreme thermomechanical working conditions, the carbide dome-celled aerogel demonstrated superelasticity across an ultrawide temperature range, spanning from 4.2 to 2273 K. We stacked six carbide aerogel plates (average density $\bar{\rho}$, 9.24 mg·cm^{-3}) and tested their compressive elasticity at 99% strain under liquid helium (4.2 K) (Fig. 3D and movie S6). The stack exhibited nearly identical compressive curves at both the 1st and 100th cycles, with no change in height. To explore the elasticity under extreme heat conditions, we transferred the same aerogel stack to an ultrahigh-temperature furnace and performed cycling compression tests in a vacuum. At 2273 K, the stack—compressed to 99% strain—recovered to its original state for 100 cycles (~2 hours). The coincident stress-strain curves at the 1st and 100th cycles confirmed the superior recoverability of our aerogels at ultrahigh temperature (Fig. 3E and movie S7) and excellent structural

stability (fig. S50). By contrast, neat graphene aerogels exhibited substantial plastic deformation at 2273 K (fig. S48F) due to the softening effect of graphene sheets at such high temperatures (*28*).

Our carbide aerogels demonstrate superelasticity at both extremely high temperatures and ultralow densities (<10 mg·cm^{-3}). We further evaluated the elasticity of these aerogels by exposing them to bilateral butane blowtorch flames in air (over 1573 K) and observed no apparent structural collapse (movie S8). The nearly coincident compressive curves at different strains (20 to 99%) and 100 repeated cycles (99% strain) confirm their excellent ablative-resisting and superelasticity (Fig. 3F and fig. S51).

Thermal superinsulation at ultrahigh temperatures

The chemical diversity of our aerogels also imparts a broad spectrum of functions (figs. S52 to S56). With their excellent high-temperature stability, our carbide aerogels offer attractive thermal superinsulation under extreme conditions. A peak anisotropic ratio ($\lambda_{horizontal}/\lambda_{vertical}$) of thermal conductivity (λ) was found at ~70% carbide content, enabling the lowest λ in the vertical direction (fig. S57). This trend can be attributed to the anisotropy of 2D topology of ultrathin walls, which facilitates the heat transport along the vertical direction and retards the thermal transport in the other horizontal direction. Our carbide aerogels presented the low λ from 173 to 2273 K (Fig. 4A) due to the

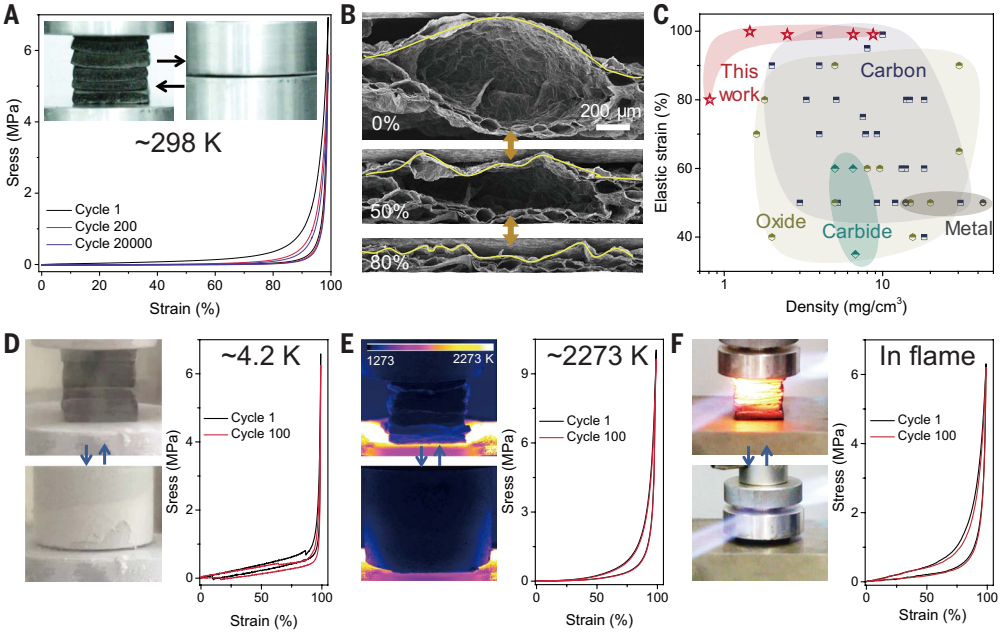

Fig. 3 Mechanical properties of dome-celled aerogels. (**A**) Compressive stress-strain curves of a stack of representative dome-celled aerogels subjected to 99% strain for 20,000 cycles at room temperature (298 K). The stacked aerogels include Al_2O_3, TaC, Cu, (TiZr)C, (AlTiCrCoNi)O, and (AlTiCrCuZnNdSmDyHfTa)O (from top), each containing ~30% graphene. (**B**) In situ SEM observations showing the vertical section of a dome cell during compression. (**C**) Plot of the maximum recoverable strain versus apparent density of dome-celled aerogels, compared with previously reported aerogels. (**D** and **E**) Compressive stress-strain curves of a stack of carbide aerogels subjected to 99% strain for 100 cycles at 4.2 K and 2273 K. (**F**) Compressive stress-strain curves of a stack of carbide aerogels subjected to 99% strain for 100 cycles in the bilateral flame of a butane blowtorch. (Inset) Experimental snapshots taken during the cycles. All stacked carbide aerogels include ZrC, TaC, TiC, (TiZr)C, (TiCrTa)C, and (ZrTiHfNbTa)C (from top).

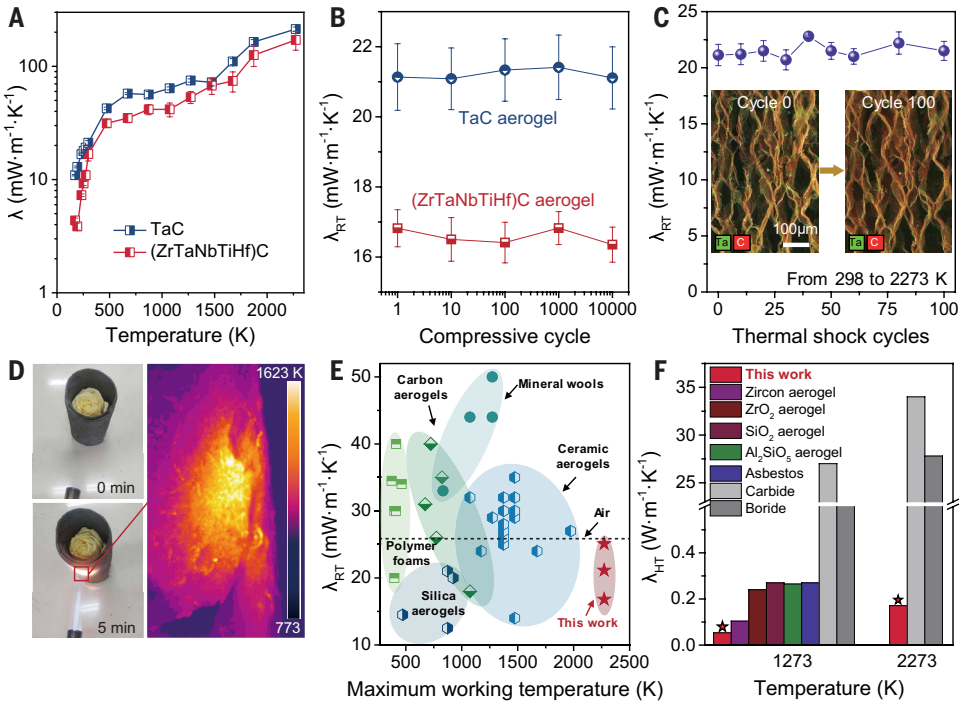

Fig. 4. Thermal superinsulation of carbide aerogels. (**A**) Thermal conductivity of TaC and high-entropy (ZrTaNbTiHf)C aerogels measured from 173 to 2273 K. (**B**) Room-temperature thermal conductivity of TaC and high-entropy (ZrTaNbTiHf)C aerogels during compression at 99% strain for 10,000 cycles. (**C**) Thermal conductivity variation of TaC aerogel during thermal shock at 2273 K (500 K s^{-1} below 1773 K and 100 K s^{-1} from 1773 to 2273 K) for 100 cycles. (Inset) Structure and elemental distribution of TaC aerogels. (**D**) Photographs illustrating the thermal protection provided by TaC aerogels and the corresponding thermal imaging map. (**E**) Comparative diagram of maximum working temperature versus room-temperature (RT) thermal conductivity (λ_{RT}) for typical insulators and our carbide aerogels (including TaC, ZrC, and high-entropy ZrTaNbTiHf carbide aerogels). (**F**) High-temperature (HT) thermal conductivity (λ_{HT}) at 1273 K and 2273 K for our carbide aerogel compared with previously reported representative ceramics.

diluted solid transport (ultralow density and nanograin boundaries), restrained gas transport with nanopores (~30 nm), and 2D anisotropy effect (figs. S58 and S59). Additionally, we found that the high-entropy (ZrTaNbTiHf)C aerogel possessed a lower λ than that of unary, binary, and ternary carbide aerogel (fig. S58D), with values of 53.4 $mW \cdot m^{-1} \cdot K^{-1}$ at 1273 K and 171.1 $mW \cdot m^{-1} \cdot K^{-1}$ at 2273 K. This high-entropy effect (*44*–*46*) was also shown by dome-celled oxide aerogels, which exhibited ultralow thermal conductivity (λ~13.4 $mW \cdot m^{-1}K^{-1}$) of (YTiLaCeNdSmGdDyEuHf oxide) in the vertical direction (fig. S52, C and D), surpassing benchmark silica aerogel and most reported insulating aerogels (*4*, *16*, *38*, *39*, *47*).

We further demonstrated that our carbide aerogels exhibit high mechanical and thermal stability. Even after mechanical fatigue tests for 10,000 cycles at room temperature and 100 cycles at 2273 K, the λ of these insulating aerogels remained stable at the ultralow level (Fig. 4B and fig. S60A), demonstrating the excellent structural stability and resistance to deformation. At 1573 K, our aerogel showed a much smaller thermal expansion coefficient (TEC) of ~1.8×10^{-6} K^{-1}, compared with a neat ceramic bulk (TEC~12.4×10^{-6} K^{-1}) (fig. S60B), further indicating the high-temperature structural stability. We then measured its thermal stability under rapid thermal shocks at an ultrahigh temperature (2273 K) using a pulse-heating furnace. The sample retained its original morphology after 100 thermal shock cycles, with nearly unchanged thermal conductivity (Fig. 4C). As a demonstration, an 8-mm-thick plate of carbide aerogel effectively protected a fresh rose when exposed to butane blowtorch flames for 5 min at temperatures exceeding 1573 K (Fig. 4D and movie S9). The mass retention ratio of carbide aerogels was ~97% after exposure to air for four hours (fig. S60C). Compared with reported high-temperature ceramic aerogels (*25*, *42*, *48*), our synthesized aerogels present a much lower λ at elevated operating temperatures up to 2273 K (Fig. 4E). The λ of carbide aerogel at high temperature is far below other aerogels and conventional insulators (Fig. 4F) (*18*, *49*, *50*), demonstrating exceptional high-temperature thermal insulating performance and reliability in extreme service environments.

In conclusion, a general graphene-based 2D channel-confined chemistry is demonstrated to fabricate a library of ultralight superelastic aerogels (194 species) with diverse materials, 35 elements, and arbitrary elemental combinations. The dome-celled microstructure imparts superelasticity even at apparent densities lower than that of air, allowing the aerogels to withstand more than 20,000 fatigue cycles at 99% strain. This ultralight aerogel library achieves both superior mechanical elasticity and ultralow thermal conductivity in a wide temperature range from 4.2 to 2273 K, considerably extending space of aerogels for extreme thermomechanics. The broad chemical diversity enables substantial design flexibility, facilitating the integration of optical, thermal, electrical, and magnetic properties.

REFERENCES AND NOTES

1. R. Wordsworth, L. Kerber, C. Cockell, *Nat. Astron.* **3**, 898–903 (2019).
2. M. Zhang *et al.*, *Science* **309**, 1215–1219 (2005).
3. S. Bag, A. F. Gaudette, M. E. Bussell, M. G. Kanatzidis, *Nat. Chem.* **1**, 217–224 (2009).
4. X. Xu *et al.*, *Mater. Today* **42**, 162–177 (2020).
5. S. S. Kistler, *Nature* **127**, 741 (1931).
6. X. Jiang, R. Du, R. Hübner, Y. Hu, A. Eychmüller, *Matter* **4**, 54–94 (2021).
7. *Aerogels Handbook*. M. A. Aegerter, N. Leventis, M. M. Koebel, Eds. (Springer, 2011).
8. N. Hüsing, U. Schubert, *Angew. Chem. Int. Ed.* **37**, 22–45 (1998).
9. J. L. Mohanan, I. U. Arachchige, S. L. Brock, *Science* **307**, 397–400 (2005).
10. W. Ma *et al.*, *Scr. Mater.* **235**, 115596 (2023).
11. L. Han *et al.*, *J. Am. Ceram. Soc.* **106**, 841–847 (2023).
12. J. T. Cahill *et al.*, *Chem. Mater.* **31**, 3700–3704 (2019).
13. N. Leventis, A. Sadekar, N. Chandrasekaran, C. Sotiriou-Leventis, *Chem. Mater.* **22**, 2790–2803 (2010).
14. M. A. Worsley, S. O. Kucheyev, J. H. Satcher Jr., A. V. Hamza, T. F. Baumann, *Appl. Phys. Lett.* **94**, 073115 (2009).
15. M. B. Bryning *et al.*, *Adv. Mater.* **19**, 661–664 (2007).
16. F. Wu, Y. Liu, Y. Si, J. Yu, B. Ding, *Nano Today* **44**, 101455 (2022).
17. L. Li *et al.*, *Nat. Commun.* **14**, 5410 (2023).
18. J. Guo *et al.*, *Nature* **606**, 909–916 (2022).
19. T. A. Schaedler *et al.*, *Science* **334**, 962–965 (2011).
20. L. R. Meza, S. Das, J. R. Greer, *Science* **345**, 1322–1326 (2014).
21. M. A. Worsley *et al.*, *J. Am. Chem. Soc.* **132**, 14067–14069 (2010).
22. Z. Xu, Y. Zhang, P. Li, C. Gao, *ACS Nano* **6**, 7103–7113 (2012).
23. M. Wu *et al.*, *Nat. Commun.* **13**, 4561 (2022).
24. L. Qiu, Z. He, D. Li, *Adv. Mater.* **30**, 1704850 (2018).
25. X. Xu *et al.*, *Science* **363**, 723–727 (2019).
26. H. L. Gao *et al.*, *Nat. Commun.* **7**, 12920 (2016).
27. Z. Xu *et al.*, *Adv. Mater.* **36**, e2401299 (2024).
28. S. Sato, H. Awaji, H. Akuzawa, *Carbon* **16**, 95–102 (1978).
29. D. Chang *et al.*, *Science* **372**, 614–617 (2021).
30. T. Mouterde *et al.*, *Nature* **567**, 87–90 (2019).
31. K. Pang *et al.*, *Sci. Adv.* **6**, eabd4045 (2020).
32. X. Bai *et al.*, *Nat. Mater.* **23**, 747–754 (2024).
33. J. Zhao *et al.*, *Science* **343**, 1228–1232 (2014).
34. Y. Yao *et al.*, *Science* **376**, eabn3103 (2022).
35. C. Oses, C. Toher, S. Curtarolo, *Nat. Rev. Mater.* **5**, 295–309 (2020).
36. Q. Zhang *et al.*, *Adv. Mater.* **29**, 1605506 (2017).
37. H. Guo *et al.*, *Adv. Mater.* **35**, e2301418 (2023).
38. C. Zhu *et al.*, *Nat. Commun.* **6**, 6962 (2015).
39. X. Cheng, Y. T. Liu, Y. Si, J. Yu, B. Ding, *Nat. Commun.* **13**, 2637 (2022).
40. L. Li *et al.*, *Mater. Today* **54**, 72–82 (2022).
41. Y. Si, X. Wang, L. Dou, J. Yu, B. Ding, *Sci. Adv.* **4**, eaas8925 (2018).
42. L. Su *et al.*, *Sci. Adv.* **6**, eaay6689 (2020).
43. S. Vinod *et al.*, *Nat. Commun.* **5**, 4541 (2014).
44. L. Gibson, M. Ashby, *Cellular Solids: Structure and Properties* (Cambridge Univ., 1997), pp. 283–307.
45. B. Notario *et al.*, *Polymer* **56**, 57–67 (2015).
46. F. Hu, S. Wu, Y. Sun, *Adv. Mater.* **31**, e1801001 (2019).
47. S. Zhao *et al.*, *Nature* **584**, 387–392 (2020).
48. L. Han *et al.*, *Nat. Commun.* **15**, 6959 (2024).
49. E. C. Schwind, M. J. Reece, E. Castle, W. G. Fahrenholtz, G. E. Hilmas, *J. Am. Ceram. Soc.* **105**, 4426–4434 (2022).
50. R. Mitra *et al.*, *J. Mater. Res.* **38**, 2122–2136 (2023).

ACKNOWLEDGMENTS

We thank G. Zhu and Y. Zeng of the Center of Electron Microscopy of Zhejiang University for assistance with performing the AC-TEM measurements. **Funding:** This work is funded by the National Natural Science Foundation of China (grants 52090031, 52090030, 52122301, 52272046, 12325204, and 12472108); National Key Research and Development Program of China (2022YFA1205300 and 2022YFA1205301); "Pioneer" and "Leading Goose" R&D Program of Zhejiang (2023C01190); Natural Science Foundation of Zhejiang Province (grant LR23E020003); and the Fundamental Research Funds for the Central Universities (grants 226-2024-00074 and 226-2024-00172). **Author contributions:** Conceptualization: K.P., Z.X., Yin.L., and C.G. Methodology: K.P., X.T.L., Z.X., Yin.L., and C.G. Investigation: K.P., Y.X., Y.X.X., X.T.L., W.H.T., X.T.L., C.Y.L., W.B.Z., Y.C., H.S.Q., W.Z.F., and L.P. Visualization: K.P., Z.X., Yin.L., Yil.L., and C.G. Funding acquisition: Z.X., Yin.L., W.W.G., H.S.Q., Yil.Li., and C.G. Project administration: Z.X. and C.G. Supervision: Z.X., Yin.L., and C.G. Writing – original draft: K.P., Z.X., and C.G. Writing – review & editing: K.P., Y.X., X.T.L., W.H.T., Z.X., Yin.L., and C.G. **Competing interests:** C.G. and K.P. are listed as inventors on a China National Intellectual Property Administration patent application filed under the Patent Cooperation Treaty (PCT/CN2025/076908, pending), which covers a preparation method for ceramic aerogels and their applications. All other authors declare no competing interests. **Data and materials availability:** All data are available in the main text or the supplementary materials.

SUPPLEMENTARY MATERIALS

science.org/doi/10.1126/science.adw5777
Materials and Methods; Supplementary Text; Figs. S1 to S60; Tables S1 to S3; References (*51*–*59*); Movies S1 to S9

Submitted 7 February 2025; accepted 23 May 2025

10.1126/science.adw5777